Available online at www.sciencedirect.com
ScienceDirect
Icarus 194 (2008) 544–561
ICARUS
www.elsevier.com/locate/icarus

Electron reflectometry in the martian atmosphere

Robert J. Lillis [a,*], David L. Mitchell [a], Robert P. Lin [a], Mario H. Acuña [b]

[a] *UC Berkeley Space Sciences Laboratory, 7 Gauss Way, Berkeley, CA 94720, USA*
[b] *NASA Goddard Space Flight Center, Greenbelt, MD 20771, USA*

Received 21 February 2007; revised 17 August 2007

Available online 8 December 2007

Abstract

The technique of electron reflectometry, a method for remote estimation of planetary magnetic fields, is expanded from its original use of mapping crustal magnetic fields at the Moon to achieving the same purpose at Mars, where the presence of a substantial atmosphere complicates matters considerably. The motion of solar wind electrons, incident on the martian atmosphere, is considered in detail, taking account of the following effects: the electrons' helical paths around the magnetic field lines to which they are bound, the magnetic mirror force they experience due to converging field lines in the vicinity of crustal magnetic anomalies, their acceleration/deceleration by electrostatic potentials, their interactions with thermal plasma, their drifts due to magnetic field line curvature and perpendicular electric fields and their scattering off, and loss of energy through a number of different processes to, atmospheric neutrals. A theoretical framework is thus developed for modeling electron pitch angle distributions expected when a spacecraft is on a magnetic field line which is connected to both the martian crust and the interplanetary magnetic field. This framework, along with measured pitch angle distributions from the Mars Global Surveyor (MGS) Magnetometer/Electron Reflectometer (MAG/ER) experiment, can be used to remotely measure crustal magnetic field magnitudes and atmospheric neutral densities at ∼180 km above the martian datum, as well as estimate average parallel electric fields between 200 and 400 km altitude. Detailed analysis and full results, concerning the crustal magnetic field and upper thermospheric density of Mars, are left to two companion papers.

Keywords: Mars; Magnetic fields; Mars, atmosphere

1. Introduction

Electron reflectometry was discovered quite accidentally in the 1970s, when Apollo subsatellite instrumentation detected suprathermal electrons traveling upward from the surface of the Moon. It was quickly realized that these were solar wind electrons which had been originally traveling toward the lunar surface but had been reflected, via the well-known magnetic mirror effect, by magnetic fields of crustal origin. The stronger the crustal magnetic field, the larger the fraction of incident electrons that were magnetically reflected before striking the lunar surface. This fraction provided a straightforward estimate of the magnetic field at the surface and this technique was used to establish some of the fundamentals of lunar crustal magnetism, e.g., enhanced magnetization at the antipodes of large, relatively young impact basins (Anderson et al., 1976; Lin, 1979).

The prime advantage of electron reflectometry over measuring magnetic fields *in situ* with orbital magnetometers is the remote sensing capability: the magnetic field is estimated at the surface of electron absorption, usually much closer to the magnetized crustal rocks. For this reason, more sensitive electron reflectometer instruments, capable of more accurately measuring the upward and downward pitch angle distributions of these electrons (pitch angle is the angle between an electron's instantaneous velocity vector and the local magnetic field), were included on the Lunar Prospector mission (Binder, 1998), further improving our understanding of lunar crustal magnetism (Halekas et al., 2001, 2002, 2003), on the failed Mars Observer mission (Acuña et al., 1992) and on its replacement, the long-lived but recently deceased Mars Global Surveyor (MGS) mission (Albee et al., 2001; Acuña et al., 2001; Mitchell et al., 2001), the analysis of data from which we will consider in this paper.

* Corresponding author.
E-mail address: rlillis@ssl.berkeley.edu (R.J. Lillis).

0019-1035/$ – see front matter
doi:10.1016/j.icarus.2007.09.030

The Magnetometer/Electron Reflectometer (MAG/ER) experiment onboard MGS (a three-axis stabilized spacecraft) consists of two triaxial fluxgate magnetometers (Acuña et al., 2001) and a hemispherical imaging electrostatic analyzer that samples electron fluxes in sixteen 22.5° × 14° sectors, spanning a 360° × 14° field of view. Electron fluxes in each sector are measured in 19 logarithmically spaced energy channels ranging from 10 eV to 20 keV. With knowledge of the magnetic field vector measured onboard, the field of view (FOV) is mapped into pitch angle (i.e., the angle between an electron's velocity vector and the local magnetic field). During a 2- to 8-s integration, the ER measures between 8% and 100% of the 0°–180° pitch angle spectrum, depending on the orientation of the magnetic field with respect to the FOV plane (Mitchell et al., 2001). The large volume of mapping orbit data, accumulated from April 1999 to November 2006, contains $>10^7$ spectra with sufficient pitch angle coverage for analysis.

Because Mars possesses a significant atmosphere, the absorbing surface for incident solar wind electrons is not solid as in the lunar case, and absorption and scattering by atmospheric neutrals occurs over a range of altitudes. The electron's path, and hence this altitude range, is determined by four main factors: the cross-sections for electron–neutral scattering, the variable density structure of the neutral atmosphere and the three-dimensional distribution of both magnetic and electric fields. In principle, upward- and downward-traveling electron pitch angle distributions measured in low orbit should be sufficient to constrain parameters describing one or more of these factors, assuming *a priori* knowledge of the other factors. But it is clear that this requires a theoretical framework that accounts for all the important physical effects to which the reflecting electrons are subject.

We have published preliminary papers explaining some aspects of this evolving framework to enable dissemination of early results (Lillis et al., 2004, 2005, 2006) and incremental improvements to that framework (Mitchell et al., 2007). However, the framework has now reached a sufficient level of maturity that it can be presented as a coherent whole to explain how these electron pitch angle distributions can be used to create sensitive, low-altitude maps of the martian crustal magnetic field, to measure electric fields in the near-Mars space environment and to monitor neutral density variations in the martian upper thermosphere.

In this paper, we explore and elucidate the technique of electron reflectometry as an investigative tool when the planetary body in question possesses a substantial absorbing atmosphere, as Mars does. We purposely start from basic concepts so that explanation of this, a new and significant adaptation of an old technique in space physics, may be accessible to those outside the field, but for whom the results may be relevant, such as solid surface geophysicists and aeronomers. After explaining the fundamentals of electron reflectometry, we present a formalism to model an electron's scattering probability given knowledge of its initial pitch angle, the magnetic field magnitude along the field line to which it is bound, the number densities of the different species of neutral molecules along its path and its energy-dependent cross sections for scattering off those molecules. Next we examine how factors in the near-Mars environment contribute to the formation of pitch angle-dependent attenuation of electron fluxes, also known as 'loss cones,' which we are to analyze. These factors include typical magnetic topologies as well as density profiles and electron impact cross sections of the dominant martian atmospheric species. Using this formalism, we develop a detailed model of loss cone formation, including parallel electric fields and atmospheric backscatter, safely ignoring plasma drifts and electron–thermal plasma interactions. We then analyze the model for altitude sensitivity and the effect of uncertainties in the magnetic and neutral density profiles. Finally, we lay out a method for how, by taking advantage of independent external measurements of the strongest crustal magnetic fields in specific geographic regions, we can solve separately and independently for the magnetic field magnitudes and neutral densities at absorption altitudes. We leave detailed explanations of, analysis by, and results from, these crustal field mapping and thermospheric density probing techniques to the two companion papers accompanying this one (Lillis et al., 2008a, 2008b).

2. Fundamentals of electron reflectometry

2.1. Electron motion in inhomogeneous magnetic fields

An electron's motion in a uniform magnetic field $\vec{B}$ is a helix whose axis is collinear with the direction of $\vec{B}$. Its velocity $\vec{v}$ can be separated into components parallel ($v_\parallel$) and perpendicular ($v_\perp$) to $\vec{B}$, where $|\vec{v}|^2 \equiv v^2 = v_\perp^2 + v_\parallel^2$. The radius of this helix, r_g, is called the gyroradius and, in SI units, is simply $v_\perp$ divided by the cyclotron frequency ω_c ($\omega_c = q_e B/m_e$, so $r_g = m_e v_\perp/(q_e B)$), where m_e and q_e are the electron mass and charge respectively and $B = |\vec{B}|$ (e.g., Parks, 2004). Typical supra-thermal solar wind electrons of interest to us at Mars have energies of ~90–400 eV (outside this range, sufficient counts for our purposes are not recorded by the MGS Electron Reflectometer due to typical electron energy spectral slopes and detector design) and typical magnetic fields at spacecraft altitudes are ~10–30 nT, giving gyroradii of ~2–7 km.

Of course, magnetic fields in the near-Mars environment are non-uniform, both spatially and temporally as the spacecraft moves in its near polar orbit and the crustal magnetic fields rotate with the planet in the solar wind. Fortunately, electron motion in such fields can be well described by conservation of the magnetic moment μ, given by

$$\mu = \frac{1/2 m v_\perp^2}{B}. \tag{1}$$

In terms of the pitch-angle α of the electron, we can write

$$\mu = \frac{1/2 m v^2 \sin^2 \alpha}{B}. \tag{2}$$

As long as ambient electric and magnetic fields are constant on a length scale which is large compared to the gyroradius and they change on a time scale which is long compared to the gyroperiod, then the magnetic moment of a charged particle is constant to very good approximation. This is known as the adiabatic condition (e.g., Parks, 2004).

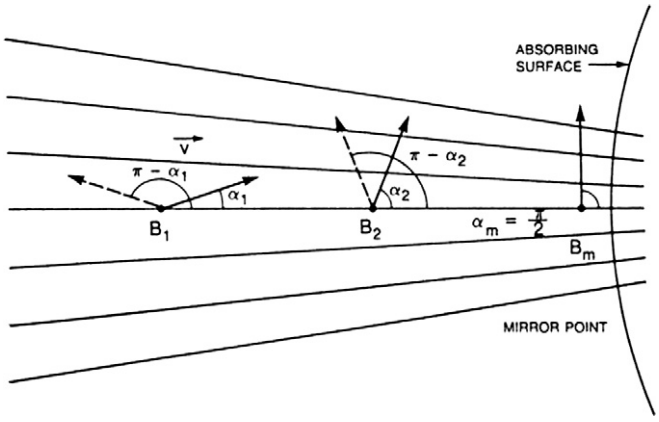

Fig. 1. Charged particle reflection in converging magnetic fields. Solid vectors are pre-reflection and dashed vectors are post-reflection. Reproduced with permission from Acuña et al. (1992).

2.2. Magnetic reflection

The conservation of magnetic moment is critically important for charged particles in regions of converging magnetic fields. Since the magnetic field magnitude B increases as field lines converge, the perpendicular velocity $v_\perp$ must also increase in order for the magnetic moment to remain constant. The parallel velocity $v_\parallel$ must therefore decrease since the total kinetic energy and hence the total velocity remains constant (in the absence of electric and other forces). If the magnetic field (and therefore $v_\perp$) increases enough, then $v_\parallel$ will decrease to zero and the particle will travel in the opposite direction, i.e. it will reflect. The magnetic field magnitude where this takes place is known as the mirror magnetic field B_m. This reflection process is illustrated in Fig. 1.

The point at which a charged particle reflects can be determined by setting the initial (represented by the subscript '0') magnetic moment equal to the magnetic moment at the reflection point, where the perpendicular velocity is equal to the total velocity,

$$\frac{1/2mv_{0\perp}^2}{B_0} = \frac{1/2mv^2}{B_m}. \tag{3}$$

But $v_\perp = v\sin\alpha$ so we may re-arrange in terms of pitch angle:

$$\sin^2\alpha_0 = \frac{B_0}{B_m}. \tag{4}$$

Thus the mirror magnetic field magnitude B_m is dependent upon the initial pitch angle and initial magnetic field. Charged particles with initial pitch angles closer to 90° than α_0 (i.e. less field-aligned) will reflect before they reach a magnetic field of magnitude B_m and those with pitch angles further from 90° than α_0 (more field aligned, i.e. closer to either 0° or 180° depending on magnetic field polarity) will reflect after. As also shown in Fig. 1, a particle with initial pitch angle α_0 will return to the same point with pitch angle $180° - \alpha_0$. Provided the distance traveled by the spacecraft during the electrons' round-trip time is less than or equal to the gyroradius (2–7 km), the incident and reflected electrons detected belong to the same plasma population and thus information contained in the plasma about the magnetic field at the mirror points is retained. For MGS MAG/ER, at ∼400 km altitude and orbiting at 3 km/s, 100–400 eV electrons have round-trip times of typically <0.3 s (see also Fig. 13), corresponding to distances of <900 m, thus the above condition is satisfied.

2.3. Determining magnetic fields remotely with pitch angle distributions

We wish to use the above formalism to determine magnetic field magnitudes at altitudes closer to the planetary surface than spacecraft orbital altitudes (∼400 km for MGS), a technique known as Electron Reflection (ER) Magnetometry or simply Electron Reflectometry. If we can measure α_0 and B_0, as we can with MGS MAG/ER, Eq. (4) tells us the magnetic field magnitude at the mirror point. However, without more information, we do not know the position along the field line at which mirroring occurs. Some absorption of the incident flux at a known altitude or altitudes, either by the planetary surface or by an atmosphere, is necessary to determine B_m at a specific location.

In the case of the Moon (or any other airless body), the situation is fairly straightforward. Let us take B_m as the field at the lunar surface. Electrons that reflect before reaching the surface will travel back up the field line, while those that would reflect after reaching the surface will strike the surface and be absorbed, except for a small fraction which Coulomb backscatter. Thus when the pitch angle distribution is measured by an orbiting spacecraft near a crustal magnetic source (as shown in Fig. 2a), the result is like that shown in Fig. 2b.

On one side of the distribution (which side depends on the magnetic field polarity), we measure downward-traveling electrons. On the other side we measure reflected, upward-traveling electrons. But these are only seen up to a certain cutoff pitch angle. Electrons with pitch angles beyond this cutoff value have struck the lunar surface before reflecting and have been absorbed, resulting in a pitch angle distribution with a sharp cutoff. The part of the distribution beyond the cutoff angle, where the incident electrons have been 'lost' to the surface, is known as a *loss cone* (this term will appear frequently from here on). By measuring this cutoff angle α_c, known as the loss cone angle, we can use Eq. (4) to determine B_m, the magnetic field magnitude at the lunar surface. This method, along with pitch angle distributions from the Lunar Prospector MAG/ER, has been used to produce a reliable, sensitive map of lunar crustal magnetic fields (Halekas et al., 2001).

The situation becomes more complex when the planetary body possesses a significant atmosphere, as Mars does. Now the absorbing surface is not a solid surface but is diffuse, so that absorption occurs over a range of magnetic reflection altitudes. The resulting loss cone is not sharp, as in the lunar case, but is 'smeared out' over a range of pitch angles. In addition, the reflected flux never goes to zero because multiple collisions between the incident electrons and atmospheric neutrals result in a significant effectively backscattered population. Fig. 3 illustrates this point. We examine only nighttime distributions because sunlight may enter the instrument aperture causing a host of undesirable effects, because non-crustal fields are

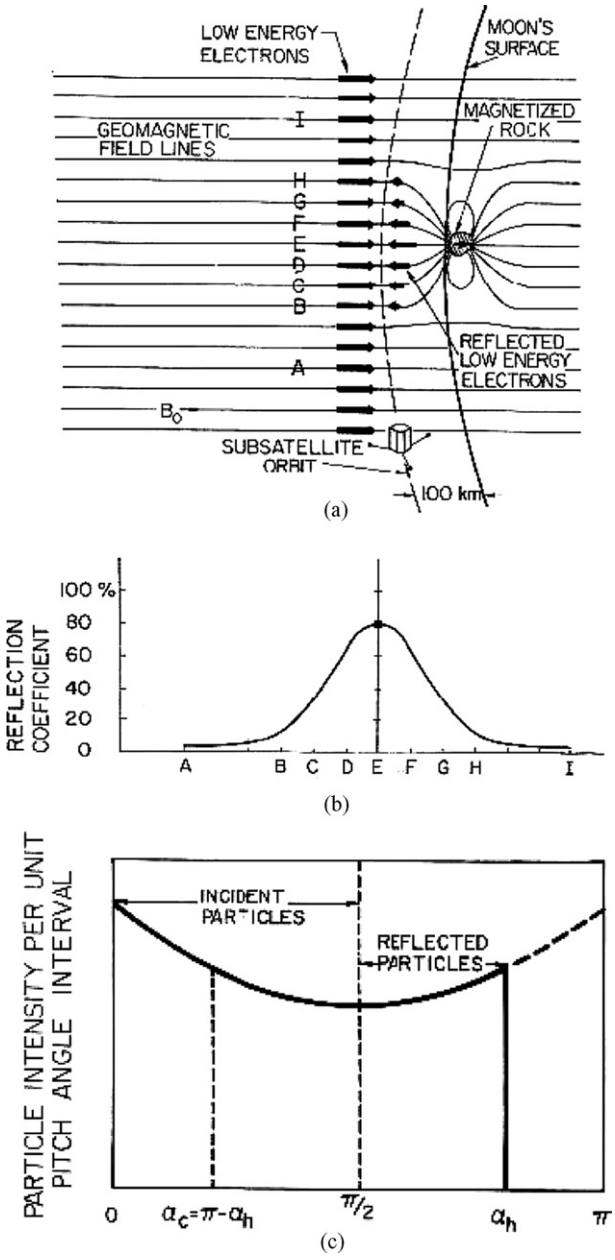

Fig. 2. (a) Schematic diagram illustrating magnetic reflection of electrons near crustal magnetic sources. The reflection coefficient is the % of down-traveling electrons that are reflected. (b) Schematic pitch angle distribution showing cut-off in reflected electron flux at angle α_h due to absorption by the lunar surface. Reproduced with permission from (Lin, 1979).

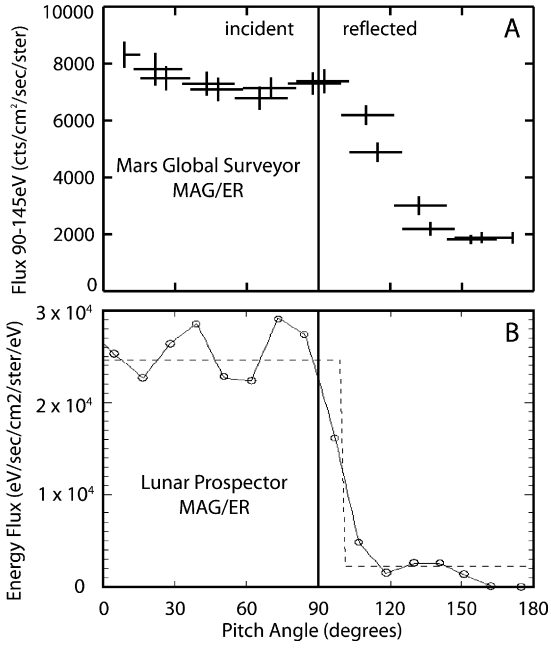

Fig. 3. Pitch angle distributions showing measured loss cones from the (A) Mars Global Surveyor and (B) Lunar Prospector Electron Reflectometers. Mars' significant atmosphere absorbs and backscatters electrons over a range of reflection altitudes, 'smearing out' and filling in the loss cone over a wide range of pitch angles. Right panel reproduced with permission from (Halekas, 2003).

more turbulent and stronger on the dayside (Brain et al., 2003; Nagy et al., 2004) and their gradients can mimic crustal fields, and because open magnetic field lines (those connected both to the interplanetary magnetic field and the martian crust) are much more common on the martian night side (Brain et al., 2007).

As a rough first attempt, we could simply measure an approximate loss cone angle (say, 120° in Fig. 3A) to determine the magnetic field at an estimated penetration depth in a simulated Mars atmosphere. However, this ignores the both the helical path of the electrons (which increases, in a pitch angle-dependent way, the effective column density through which the electron passes) and the shifting and infilling of the loss cone caused by backscatter. The error would not be quantifiable without investigating these effects.

Therefore, our approach shall be to investigate in detail the motion, through an extended neutral atmosphere, of suprathermal (90–400 eV) electrons in converging magnetic fields. This will allow us to develop a model of loss cone formation, the parameters of which can be constrained by least-squares fitting with respect to measured loss cones, such as Fig. 3A. If a specific atmospheric model is assumed, we can constrain the magnetic field magnitude at the absorption altitudes, as was a primary objective of the MAG/ER experiment (Acuña et al., 1992). Conversely, if a model is assumed for the magnetic fields, we can also constrain neutral densities at the absorption altitudes, an unexpected bonus measurement, though somewhat difficult to implement (Lillis et al., 2005, 2008a).

3. Model of electron–neutral scattering

Consider a beam of particles of intensity I (in units of particles $\mathrm{m}^{-2}\,\mathrm{s}^{-1}$) traveling through a scattering medium of number density n. Let each scatterer present an effective scattering cross-sectional area σ. The number of scatterers in a volume element of length $\mathrm{d}s$ and area $\mathrm{d}A$ perpendicular to the beam direction is $(n\,\mathrm{d}A\,\mathrm{d}s)$, presenting a cross-sectional area of $(\sigma n\,\mathrm{d}A\,\mathrm{d}s)$. Thus the total number of particles scattered in that volume element in time $\mathrm{d}t$ is given by $I\,(\sigma n\,\mathrm{d}A\,\mathrm{d}s)\,\mathrm{d}t$. This can also be written in terms of the differential change in intensity as

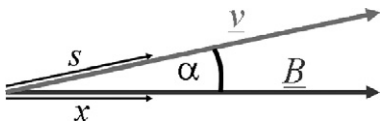

Fig. 4. Illustration showing the relationship between helical path s and guiding center path x in terms of pitch angle α, electron velocity v, magnetic field B.

$\mathrm{d}I\,\mathrm{d}A\,\mathrm{d}t$. Setting these equal gives

$$\mathrm{d}I\,\mathrm{d}A\,\mathrm{d}t = -I\sigma n\,\mathrm{d}A\,\mathrm{d}s\,\mathrm{d}t \quad \Rightarrow \quad \frac{\mathrm{d}I}{\mathrm{d}s} = -n\sigma I \tag{5}$$

with a minus sign because the intensity is decreasing as particles are scattered out of the beam. Solving this equation gives the beam intensity as a function of distance traveled along a path $s_0 \rightarrow s$ through the scattering medium.

$$I(s) = I(s_0)\exp\left[-\sigma\int_{s_0}^{s} n(s')\,\mathrm{d}s'\right]. \tag{6}$$

Therefore the probability $P(s)$ of any particle in the beam *not* being scattered over the same distance s is given by $I(s)/I(s_0)$. We shall label this the *survival* probability P_{surv}. Also, since the atmosphere of Mars consists of more than one type of molecule, we need to account for more than one type of scatterer by summing the exponent over the different neutral species i. Hence we can write

$$P_{\mathrm{surv}}(s,U) = \frac{I(s)}{I(s_0)} = \exp\left[-\sum_i \sigma_i(U)\int_{s_0}^{s} n_i(s')\,\mathrm{d}s'\right] \tag{7}$$

where U is the energy of the electron and $\sigma_i(U)$ is the energy-dependent cross-section for electron scattering off atmospheric species i. As discussed in Section 2, the path followed by an electron through the atmosphere is a helix of variable radius and pitch angle, while n_i, the number density of atmospheric species i, is generally defined as a function of altitude h above a surface of constant gravitational potential, called the *datum*. Therefore we must recast Eq. (7) in terms of a variable common to both the electron's path length variable s and its altitude h. The simplest choice is the distance traveled by the electron along the magnetic field line to which it is bound, often referred to as the guiding center path variable or GCP, denoted x. For every distance $\mathrm{d}s$ traveled along the helical path, an electron travels a distance $\mathrm{d}x = \mathrm{d}s\cos\alpha$ along the guiding center path, where α is the electron's pitch angle, as shown in Fig. 4.

Also, provided we know the magnetic field line geometry (i.e. field strength and direction as a function of altitude), we can directly relate altitude h to x and determine $n_i(x)$. With these two relations we can now express P_{surv} in terms of an integral

$$P_{\mathrm{surv}}(x,U) = \exp\left[-\sum_i \sigma_i(U)\int_{x_0}^{x} n_i(x')\sec\alpha(x')\,\mathrm{d}x'\right]. \tag{8}$$

We then make use of the conservation of magnetic moment (Eq. (2)) to relate the pitch angle α_0 and magnetic field magnitude B_0 at the initial position x_0 to that at any point x along the guiding center path:

$$\sin^2\alpha(x) = \frac{B(x)}{B_0}\sin^2\alpha_0. \tag{9}$$

Substituting for $\alpha(x)$ in Eq. (8), we arrive at an expression for an electron's probability of surviving (i.e. not scattering) after traveling a distance x along a magnetic field line of varying magnitude B, through a gas of multiple species i and varying density n:

$$P_{\mathrm{surv}}(x,U) = \exp\left[-\sum_i \sigma_i(U)\int_{x_0}^{x} \frac{n_i(x')\,\mathrm{d}x'}{\sqrt{1-\frac{B(x')}{B_0}\sin^2\alpha_0}}\right]. \tag{10}$$

4. Factors affecting loss cone formation in the near-Mars environment

In addition to the above formalism describing electron scattering probability, we also need to examine the real conditions in the near-Mars space environment, i.e. the magnetic fields and absorbing atmosphere that form the loss cones we measure with the MGS MAG/ER, so we can understand how to appropriately model their formation.

4.1. Magnetic topology in near-Mars space

As well-described in the review by Nagy et al. (2004), the large-scale magnetic field topology in the vicinity of Mars is dominated by the draping of the interplanetary magnetic field (IMF) around the planet into an induced 2-lobed magnetotail as a result of the solar wind encountering the conducting obstacle of Mars' dayside ionosphere. This interaction between Mars and the interplanetary medium results in three main distinct magnetic field configurations encountered by MGS in its polar orbit at 400 km altitude, at 2 a.m./2 p.m. local time, as shown in Fig. 5. Closeup examples of each and the pitch angle distributions resulting from them are shown in Fig. 6.

4.1.1. 'Unconnected'

On most of the dayside and often on the night side near the terminator, the draped IMF lies approximately parallel to the local horizontal and does not connect to the martian crust (see label '1' in Fig. 5). Hence, electrons on such field lines never encounter the absorbing neutral atmosphere and loss cones never form. Thus pitch angle distributions are nearly flat (see Fig. 6, top).

4.1.2. 'Closed'

In regions of strong crustal magnetism, field lines form closed loops, attached at both ends to the magnetic crust (see label '2' in Figs. 5 and 6, middle). Solar wind electrons have no direct access to these lines, causing either plasma voids with extremely low electron fluxes (2–3 orders of magnitude below typical fluxes) or, where electrons from nearby open or unconnected field lines may drift onto closed field lines, 'mirror' pitch angle distributions (often called 'double-side loss cones'),

which are caused by electrons making multiple reflections on the same field line (see Fig. 6, middle right). Such distributions will narrow with time as the neutral atmosphere absorbs electrons near the edges of the distribution. Since we cannot tell when they formed, modeling them as we do one-sided loss cones is not possible.

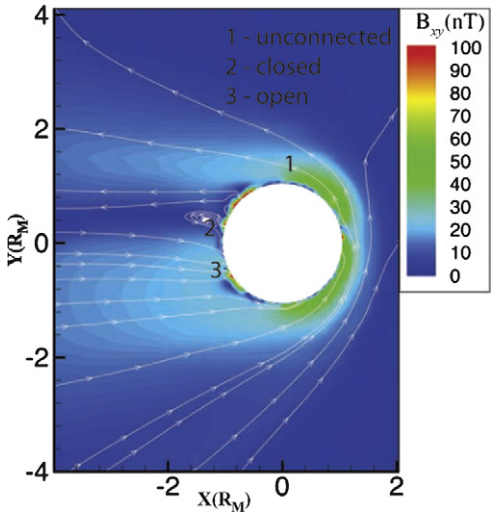

Fig. 5. MHD simulation of the near-Mars magnetic environment, shown in the Mars solar ecliptic coordinate system where $+X$ is toward the Sun and $+Z$ is upward out of the plane of the ecliptic. The magnetic field lines are shown by white lines with arrows and the color scale represents the magnitude of the component of the magnetic field in the XY plane. The numbers 1, 2 and 3 represent the main three distinct magnetic topologies encountered by Mars Global surveyor in its polar orbit at 2 a.m./2 p.m., as discussed in the text. Reproduced with permission from Ma et al. (2002).

4.1.3. 'Open'

On the night side, magnetotail field lines above crustal magnetic fields lie approximately in a sunward/anti-sunward direction. Almost always in regions of weak or moderate crustal fields and in strong crustal field regions when the magnetic topology allows (i.e. 'cusps,' see label '3' in Figs. 5 and 6, bottom), these field lines connect both to the crust and the IMF. This allows solar wind electrons to travel down the magnetotail and precipitate onto the atmosphere. As described in the previous section, this results in a one-sided loss cone (see Fig. 6, bottom). It is these night side distributions we use for analysis.

In this paper, we shall be making the 'vacuum field assumption' regarding magnetic fields in near-Mars space, i.e. that the fields whose sources are within the planet may be added vectorially to the external magnetic field which is 'frozen-in' to the plasma (due to the very high plasma conductivity; see Parks, 2004) surrounding the planet, flowing with this plasma and causing the aforementioned draping effect. This ignores the effects of plasma waves of comparable period to the electron bounce time (<0.3 s). Espley et al. (2006) have shown that waves between 0.1 and 1 Hz observed in the near-Mars environment typically have amplitudes of <0.5 nT, negligible compared with the magnetic field magnitudes of 10–500 nT encountered by the incident solar wind electrons on the martian night side that we consider. It also ignores magnetic discontinuities due to magnetic reconnection between the interplanetary magnetic field and the crustal fields (which must occur at Mars for solar wind electrons to be observed for the second and third topologies listed above) and the existence of current sheets. However, the former is expected to be, and the latter has been shown to be, extremely localized (Halekas et al., 2006)

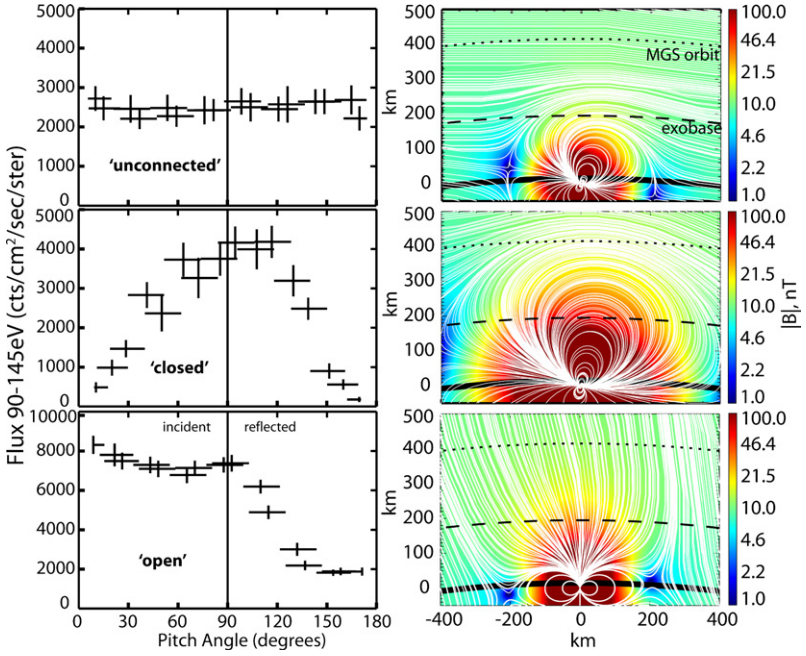

Fig. 6. On the left are illustrative pitch angle distributions from the MGS MAG/ER experiment, resulting from the three primary magnetic topologies observed on the martian night side: unconnected, closed and open, as described in the text below. On the right are corresponding schematic diagrams of these topologies showing the field lines resulting from the superposition of a 10 nT ambient 'background' magnetotail field with that of typical dipolar crustal magnetic sources. The dotted line is the MGS 400 km orbit and the dashed line represents the approximate altitude of the exobase (i.e. the boundary between collisional and collisionless atmospheric regions) at 180 km.

and therefore can be ignored in a statistical sense. With these assumptions, the techniques to be described seem to work remarkably well when confined to the martian shadow, where magnetic conditions are significantly quieter than in sunlight (Ferguson et al., 2005).

4.2. The martian nighttime upper atmosphere

Simple range calculations show that solar wind electrons in our energy range of interest (90–400 eV) do not penetrate Mars' atmosphere below 140 km altitude (Acuña et al., 1992), hence we are interested only in the region above this, known as the middle-to-upper thermosphere, which has been sampled by several spacecraft. The only species-specific measurements were provided by the Viking 1 and 2 landers, whose mass spectrometers yielded two vertical profiles below 200 km (Nier and McElroy, 1977). Accelerometers on board the Mars Global Surveyor & Mars Odyssey orbiters provided 1600 and 600 vertical mass density profiles respectively from 100 to 170 km during aerobraking (Withers, 2006). More sensitive accelerometers on Mars Reconnaissance Orbiter provided mass densities up to 170 km (Bougher et al., 2007), though these data are not publicly available at the time of writing. Based on these measurements and incorporating much of the relevant physics and atmospheric chemistry, thermospheric global circulation models or TGCMs have been developed to simulate winds, temperatures and densities as a function of altitude, latitude, longitude, season and local time. For the purposes of this electron modeling effort, we use results from the Mars Thermospheric Global Circulation Model (e.g., Bougher et al., 1990, 1999, 2000, 2002, 2006), simulated for solar moderate EUV flux, equinox conditions at the equator at MGS' local night time of 2 a.m. CO_2 and O are the dominant species with the others accounting for up to 8% of the total density, depending on altitude. Its nighttime density predictions can vary by more than an order of magnitude from solar minimum conditions at aphelion to solar maximum conditions at perihelion. With such a wide range of conditions to simulate and a comparatively small amount of data with which to compare, the MTGCM is often unconstrained and thus can have large uncertainties (factor of three to four) particularly at altitudes above ∼160 km where the influence of the impacting solar wind can be significant.

4.3. Electron–neutral impact cross-sections

Accurate laboratory measurements and quantum theoretical calculations of energy-dependent cross-sections for electron impact on neutral gases are important for studies of subjects as diverse as planetary surface dust-charging, human radiation exposure, noble gas lasers and atmospheric auroral emission. When a primary incident electron strikes a neutral molecule, its kinetic energy is partitioned between several possible processes: (1) kinetic energy of the escaping primary, (2) kinetic energy of the molecule (negligible due to the large difference in their respective masses), (3) change in the electronic state of the molecule, (4) unbinding of one or more molecular electrons, (5) kinetic energy of newly-unbound electrons and (6) dissociation of the target molecule.

For our purposes, we require cross-sections and associated primary electron energy losses for all the observed combinations of processes 3–6 for each neutral species as well as the distribution of primary electron scattering angles. This allows us to model the pitch-angle evolution and energy degradation of the incident electrons. Total cross-sections are also needed to calculate total scattering probabilities.

The literature on this subject is extensive but we were able to develop a comprehensive database of cross-sections for O, O_2, N_2, CO_2, CO and Ar from Ajello et al. (1990), Cvejanovic and Crowe (1997), Chilton and Lin (1999), Itikawa (2002) and the impressive compilation of Sung and Fox (2000). Differential cross-sections for secondary electron emission were obtained from Shyn and Sharp (1979), Burnett and Rountree (1979) and Opal et al. (1971) and angle-dependent relative scattering cross-sections were obtained from Porter and Jump (1978) and Porter et al. (1987). As an illustration, Fig. 7 shows total scattering cross-sections. Uncertainties differ substantially across this wide range of cross-sections but are typically in the range 20–30%, which result in predicted loss cone shifts of $<1^\circ$ and can thus be safely ignored.

5. Loss cone model

Using the scattering formalism in Section 3, we now present a model for loss cone formation, the parameters of which may be constrained by least-squares fitting to measured loss cones, like that shown in the bottom panel of Fig. 6. After first presenting a simple adiabatic loss cone model, we shall amend it to include the effects of parallel electric fields and atmospheric backscatter.

5.1. Adiabatic loss cone model

The assumption of our basic loss cone model is simple, that all electrons incident on the atmosphere are either lost to the atmosphere (i.e. scattered) or remain adiabatic (that is to say their magnetic moment is conserved throughout their entire trajectory). Therefore we can use Eq. (10) directly to predict what fraction of downward electron flux observed by the spacecraft at pitch angle α_0 will return to the spacecraft at angle $180^\circ - \alpha_0$ after magnetically reflecting. The path taken is then from $x = 0$ at the spacecraft to $x = x_r$, the reflection point, which is found, assuming we know $B(x)$, by solving for x_r in

$$B(x_r) = \frac{B_0}{\sin^2 \alpha_0}. \tag{11}$$

Since the electron's return trajectory from the reflection point is a mirror image of its downward trajectory (see Fig. 1), we simply multiply the exponent in Eq. (10) by a factor of 2 to get an equation describing an adiabatic loss cone:

$$P_{\text{surv}} = \exp\left[-2\sum_i \sigma_i(U) \int_0^{x_r} \frac{n_i(x')\,\mathrm{d}x'}{\sqrt{1 - \frac{B(x')}{B_0}\sin^2\alpha_0}}\right]. \tag{12}$$

It will later be useful to think of the negative exponent in Eq. (12) as a dimensionless 'scattering depth' for electrons (akin to an optical depth for photons) as they travel in a helical path from the spacecraft to the reflection point and back. We denote this scattering depth D. Expressing P_{surv} in terms of D:

$$P_{\text{surv}} = \exp[-D],$$
$$D = 2\sum_i \sigma_i(U) \int_0^{x_r} \frac{n_i(x')\,\mathrm{d}x'}{\sqrt{1 - \frac{B(x')}{B_0}\sin^2\alpha_0}}. \tag{13}$$

Fig. 8 illustrates this model for the 145–248 eV channel of the ER instrument, showing how an electron's pitch angle and cumulative scattering probabilities change with altitude as it travels down, reflects, then travels up along a vertical magnetic field line, given its initial pitch angle and a magnetic field and density profile. It also shows the resulting loss cone shape, as calculated by the adiabatic model.

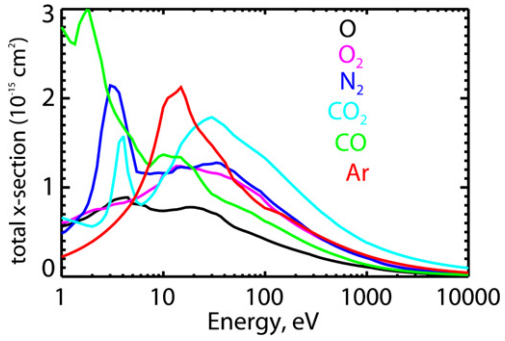

Fig. 7. Total electron–neutral scattering cross-sections. Though plotted for all energies between 1 eV and 10 keV, only those over ~100 eV are important for our purposes.

5.2. *Parallel electric fields*

The next consideration is that of magnetic field-aligned or 'parallel' electric fields, which accelerate/decelerate the electrons we measure, changing their pitch angles and reflection altitudes (perpendicular electric fields cause plasma drifts and will be considered in Section 6). Since there are no direct electric field measurements at Mars and since such electric fields should affect loss cone shapes, we must amend our model to include this effect in the event that these fields turn out to be significant.

Parallel electric fields alter electron energies and pitch angles, making the loss cone formation process much more strongly energy-dependent than it is in the absence of such fields (the energy dependence of the cross sections causes a very small shift, $<1°$, in predicted loss cones between different energies in our range of interest, 90–400 eV).

Consider an electron's total energy at points 1, 2 along the same field line with electrostatic potentials V_1, V_2 and magnetic field magnitudes B_1, B_2. All forces are conservative so this total energy should be conserved:

$$\frac{1}{2}mv_1^2 - eV_1 = \frac{1}{2}mv_2^2 - eV_2. \tag{14}$$

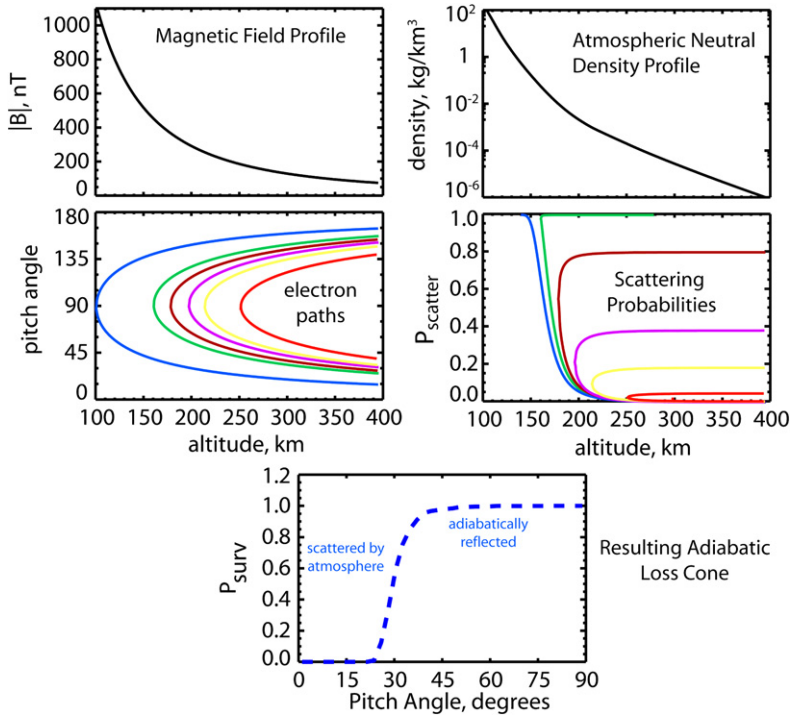

Fig. 8. Left side: a typical magnetic field–altitude profile for a region of strong crustal field and the paths it dictates for electrons starting at 6 different pitch angles: 15, 24, 27, 30, 33, 40 degrees. Right side: a typical mass density–altitude profile and the cumulative scattering probabilities it dictates for 191 eV electrons as they travel down in altitude and back up again. Bottom: the loss cone shape which results from the same magnetic field and density profile, calculated using the adiabatic model.

Also recall that the magnetic moment μ, which is dependent on the component of the electron's velocity perpendicular to the magnetic field, is not affected by the parallel electric field and so is still conserved:

$$\Rightarrow \quad \mu_1 = \frac{\frac{1}{2}mv_{1\perp}^2}{B_1} = \frac{\frac{1}{2}mv_{2\perp}^2}{B_2} = \mu_2,$$

$$\Rightarrow \quad \frac{\frac{1}{2}mv_1^2\sin^2\alpha_1}{B_1} = \frac{\frac{1}{2}mv_2^2\sin^2\alpha_2}{B_2},$$

$$\Rightarrow \quad \sin^2\alpha_2 = \frac{v_1^2}{v_2^2}\frac{B_2}{B_1}\sin^2\alpha_1. \tag{15}$$

Combining Eqs. (14) and (15) we obtain:

$$\sin^2\alpha_2 = \frac{B_2}{B_1}\frac{\sin^2\alpha_1}{\left(1+\frac{2e(V_2-V_1)}{mv_1^2}\right)}. \tag{16}$$

Now if we re-label in terms of distance x traveled along a magnetic field line, define $\Delta V(x) = V(x) - V_0$ and let $U_0 = \frac{1}{2}mv_0^2$ be the kinetic energy of the electron, we obtain

$$\sin^2\alpha(x) = \frac{B(x)}{B_0}\frac{\sin^2\alpha_0}{\left(1+\frac{e\Delta V(x)}{U_0}\right)}. \tag{17}$$

One can understand this intuitively by considering that if $\Delta V(x) > 0$ then the electric field is in the $-x$ direction, accelerating the negatively charged electron in the $+x$ direction, increasing its parallel velocity but leaving its perpendicular velocity unchanged and hence changing its pitch angle $\alpha(x)$ further from 90° than it would be if no electrostatic potential existed. The opposite is true if $\Delta V(x) < 0$. See Fig. 9 for an illustration. Note that Eq. (17) reduces to Eq. (9) in the case where $\Delta V(x) = 0$. Note also that if the denominator in brackets becomes negative, the equation becomes meaningless, i.e. the electron cannot exist at this point x because it has already reflected.

We can use Eq. (17) to modify Eq. (13) to arrive at an expression for the survival probability of an electron traversing a given magnetic and atmospheric density profile while being accelerated along a magnetic field line by an electrostatic potential $\Delta V(x)$, with the energy-dependent scattering cross section now inside the integral. We keep the factor of two outside the summation sign from Eq. (13) because, as we have mentioned, the electric and magnetic forces are conservative and therefore an electron will have the same energy at a given altitude whether it is traveling upwards or downwards and so the inbound and outbound trips involve passage through the same column depth of atmosphere.

$$P_{\text{surv}} = \exp\left[-2\sum_i \int_0^{x_r} \frac{\sigma_i(U_0 + e\Delta V(x'))n_i(x')\,dx'}{\sqrt{1-\frac{B(x')\sin^2\alpha_0}{B_0(1+\frac{e\Delta V(x')}{U_0})}}}\right]. \tag{18}$$

Thus, in planetary coordinates, a radially positive (negative) electric field will cause electrons to reflect lower (higher) than they would otherwise, with a larger effect for lower energies (i.e. a larger fraction in the denominator of Eq. (18)). The result is that parallel electric fields influence loss cone shapes

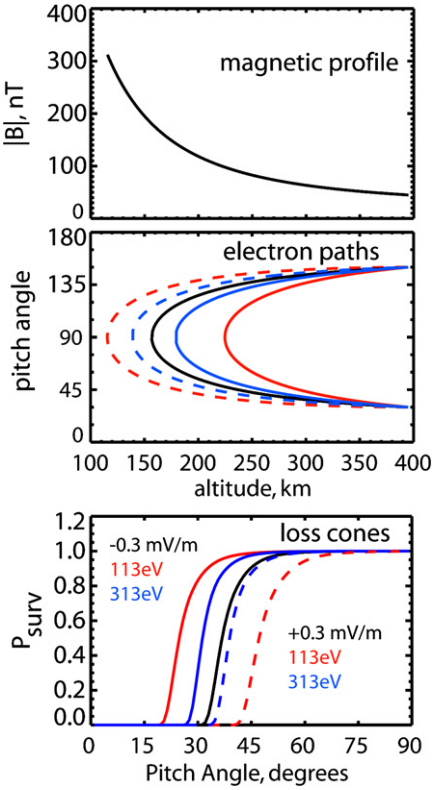

Fig. 9. Effect of parallel electric fields on electron paths and loss cones. Pitch angle–altitude trajectories (for identical initial pitch angles) and resultant loss cones are plotted for 113 eV (red) and 313 eV (blue) electrons for a constant, radially positive (dashed lines) and negative (solid lines) parallel electric fields of 0.3 mV/m. In black is plotted the energy-independent trajectory and loss cone with no parallel electric fields.

in an energy-dependent way, as illustrated in Fig. 9. To detect the presence of such fields, we require loss cone measurements in at least 2 energy channels. With a single channel, the effects of a radially positive field may be indistinguishable from a weaker crustal magnetic field or a thicker atmosphere. This energy dependence can be used to simultaneously solve for both the electric field and the crustal magnetic field. As a starting point and to reduce the number of parameters to solve for, we assume a constant electric field component parallel to the magnetic field line below the spacecraft, i.e. $V(x) = kx$, where k is a positive or negative constant. Since, as it will turn out, electrons are absorbed over quite a narrow range of altitudes, more complicated electrostatic potential or electric field profiles would be very difficult to distinguish from simple profiles anyway. As shown in Fig. 9, fields smaller than 1 mV/m can have a substantial effect on loss cone shapes.

Parallel electric fields play an important role in the plasma and dynamics of the near-Mars environment because they can drive currents and can aid or hinder electron precipitation along open field lines, affecting energy deposition and auroral processes in the martian upper atmosphere. While electron reflectometry is sensitive only to the total electric potential between the spacecraft and the exobase, these measurements should still be useful in helping to characterize the location and magnitude of the electron acceleration processes which

operate in the martian night hemisphere (Brain et al., 2006; Lundin et al., 2006).

5.3. Atmospheric backscatter

Another consideration is that of atmospheric backscatter. We should not expect the martian atmosphere to be a perfect absorber and indeed it is not. Incident solar wind electrons scatter off neutrals, thereby altering their pitch angles and losing some of their kinetic energy to atomic processes. A certain fraction will be effectively backscattered up toward the spacecraft, partially 'filling in' the loss cone and therefore shifting it. To account for this, the backscattered population must be correctly modeled. We outline this model below and show how to use it to subtract the backscattered population of electrons so that we can apply the adiabatic model explained in Section 3 to constrain the atmospheric density and the remote magnetic field.

5.3.1. Monte Carlo modeling of electron loss cones

Here we treat the electron motion more comprehensively. For each electron, the starting position is at the spacecraft altitude with any desired pitch angle and energy. Equation (18) is used to calculate the cumulative probability for a collision as a function of distance along the electron's helical path, as shown in the middle right panel of Fig. 8. A random number is used to determine where along the path, if at all, a collision occurs. If so, the electron's position and pitch angle immediately beforehand are recorded, a second random number determines which neutral species the electron strikes according to the separate probabilities for collision with each species (from Eq. (18)) and a third determines what scattering process occurs (e.g., elastic collision, dissociation, excitation or ionization) and determines the associated energy loss of the impacting electron, according to the relative cross-sections for each process. For ionizations, the energy loss resulting from the range of possible secondary electron energies is accounted for by treating as separate processes the emission of secondaries in 25 discrete energy bins logarithmically from 1 to 100 eV. A fourth random number determines the polar scattering angle according to angular scattering functions from Porter and Jump (1978) and Porter et al. (1987) and a fifth randomly determines the azimuth scattering angle. The initial pitch angle and polar and azimuthal scattering angles determines the post-collision pitch angle. A new helical trajectory is calculated, and the Monte Carlo procedure is repeated until the particle either 'escapes' the atmosphere (meaning its altitude exceeds that of the spacecraft while traveling upwards) or its energy falls below some threshold, usually the lower bound of a given energy channel. The secondary electrons themselves are ignored because their energies are never high enough to be counted in the three energy channels which we analyze, spanning 90–400 eV.

The input energy spectrum is taken to be the mean of all spectra measured outside of crustal field-induced plasma voids (Mitchell et al., 2001) over a typical four-day period of quiet conditions in the night hemisphere (i.e. stable interplanetary magnetic field, stable solar wind flux and no unusual solar activity) from June 19–23, 1999. Typically 100,000 electrons with appropriate energies to match the input spectrum, equally distributed in pitch angle, are sent down the pre-determined field line towards the atmosphere and simulated spacecraft pitch angle distributions at 400 km (shown in Fig. 10) are built up. This method is $\sim 10^6$ times slower than the adiabatic method, usually requiring several tens of minutes to calculate a single loss cone shape accurately.

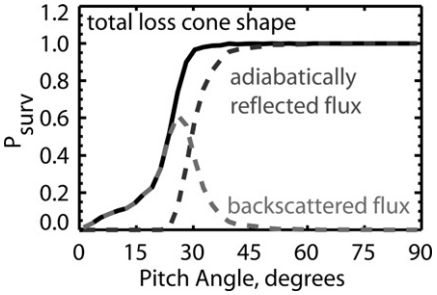

Fig. 10. The loss cone shape which results from the same magnetic field and density profile as in Fig. 8, calculated using the adiabatic model (dotted line) and full Monte Carlo model (black solid line). The backscattered population (dashed line) is the difference between the two model curves.

5.3.2. Backscatter subtraction

Clearly we would like to include the backscatter effect in fitting the observed loss cones to constrain neutral densities and field magnitudes, but using the full Monte Carlo model would be prohibitively time-consuming. Therefore we must devise a method of subtracting the backscattered component from any given observed loss cone before using the adiabatic model for analysis.

This is possible because, to a good approximation, for any pitch angle, the fraction of the observed flux which has been backscattered is a function only of the total scattering depth of atmosphere through which an electron (with that starting pitch angle) passes along its helical path, regardless of the details of the atmospheric and magnetic profiles (as shown in Fig. 11, bottom right). We have run Monte Carlo simulations for a range of uniform parallel electric field values from -0.5 to 0.5 mV/m and find this to be true except in cases where the combination of a weak magnetic gradient and a strong radially positive parallel electric field prevent any upward-traveling adiabatic electrons from reaching spacecraft altitude.

Thus a look-up table of fully calculated Monte Carlo loss cones and their adiabatic counterparts, calculated for a complete range of possible magnetic profiles (as shown in Fig. 11) and values of parallel electric field from -0.5 to 0.5 mV/m, is sufficient, with appropriate interpolation, to represent the very great majority of loss cones we will encounter in the dataset. For a given observed loss cone, we define the 'loss cone angle' to be the pitch angle where P_{surv} is equal to 65% (somewhat arbitrary but high enough to avoid the 'backscatter tail' and ensure a single value no matter how pathologic the pitch angle distribution) and we determine this loss cone angle separately for all 3 energy channels: 90–145, 145–248, 248–400 eV. Using least-squares fitting to compare these observed loss cone angles to loss cone angles in the lookup table,

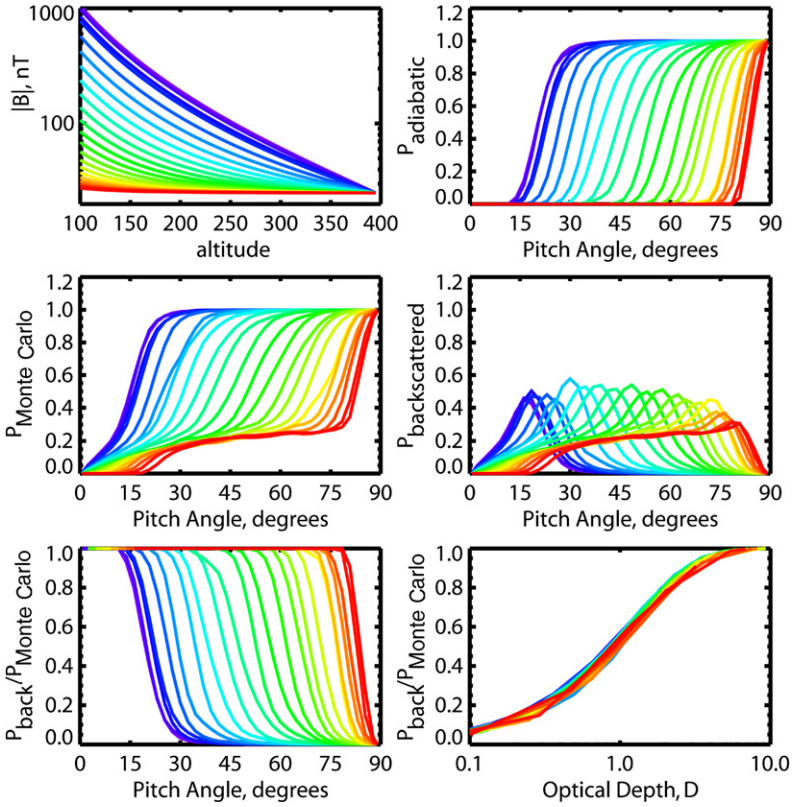

Fig. 11. For a range of 23 different magnetic profiles (top left) and a typical atmospheric profile, we plot the corresponding loss cones using the adiabatic model (top right) and the full Monte Carlo model (middle left). We also plot the backscattered flux (middle right). The two bottom plots show the ratio of the backscattered flux to the total, flux plotted vs pitch angle (left) and scattering depth (right). Within the statistical noise of the Monte Carlo simulation, this ratio is only a function of scattering depth of atmosphere and not of any of the separate details of the atmospheric and magnetic profiles.

we calculate which set of precalculated loss cones best correspond to the observed loss cones. These precalculated loss cones correspond to arrays of pitch angles and associated values of $P_{\text{backscatter}}/P_{\text{Monte Carlo}}$ (see Fig. 11, bottom left), i.e. fractions of the flux to be subtracted for every pitch angle. We do this, convolving from 50 model pitch angle bins to the 8 upward-traveling instrumental pitch angle bins (e.g., right half of Fig. 3A) that can vary in width and position. After this subtraction, we are left with our best representation of the adiabatic loss cone shape, i.e. what the shape of the loss cone would be if every collision with an atmospheric neutral molecule resulted in the absorption of the electron. A sample subtraction is shown in Fig. 12.

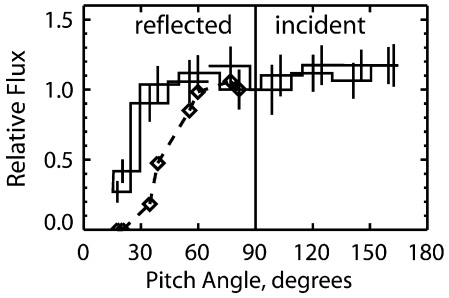

Fig. 12. Sample backscatter subtraction. The solid black line shows a typical loss cone pitch angle distribution in the 116 eV energy channel. The dark gray diamonds and dashed line show the flux levels after the backscattered flux has been subtracted, leaving behind the best representation of the adiabatic loss cone.

6. Ignored physical considerations

So far we have analyzed in detail a loss cone model that promises to be useful in constraining remote magnetic fields and atmospheric neutral densities. However, this model is quite idealized, so before it can be applied to real data, we need to examine the physical details it ignores to determine their importance. If unimportant, they may be safely omitted.

6.1. Electron Coulomb losses to the surrounding plasma

The first serious physical consideration is that of the incident electron's energy loss to the ambient thermal plasma, given in the following formula adapted from Dalgarno et al. (1963), using the formalism of Butler and Buckingham (1962):

$$\frac{\mathrm{d}U}{\mathrm{d}x} \cong -2 \times 10^{-7} \frac{n_e}{U} \text{ eV/km}, \tag{19}$$

where U is the energy of the incident electron in eV, $\mathrm{d}U/\mathrm{d}x$ is its rate of change of energy with respect to distance traveled in electron volts per kilometer and n_e is the ambient thermal plasma density in cm^{-3}. The 'constant' in the above formula is proportional to the square root of the electron temperature, which may be a factor of 2 to 3 lower for the martian night side

ionosphere compared to the earth's (for which the formula was derived). However, a brief look at this energy loss with some typical numbers shows that it may be safely ignored in our modeling. If we take the case of the lowest energy incident electron we shall consider and the highest measured martian ionospheric density (Tyler et al., 2001), 90 eV and 3×10^5 cm^{-3} respectively, we arrive at an energy loss of less than 600 μeV/km, completely negligible. Thus we feel justified in ignoring this effect.

6.2. Plasma drifts

As mentioned in Section 2, we must be certain we are observing approximately the same population of electrons spiraling towards the planet and back up to the spacecraft. Separate from its gyromotion around, and linear motion along magnetic field lines, any charged particle in the presence of external forces (i.e. gravity or electric fields) or inhomogeneous magnetic fields will experience a drift across magnetic field lines, the detail of which depends on the curvature and gradient of the magnetic field and the field's direction relative to the external forces (see Parks, 2004). These drifts are primarily caused by the particle's changing gyroradius as either B or v is different during different parts of the particle's orbit.

It is important to point out that, although changes in magnetic topology (i.e. a transition from open to closed field lines) happen over length scales as small as an electron gyroradius (<5 km; Mitchell et al., 2001), because its source is mainly in the crust, lateral variations in the magnetic field encountered by the electrons are peaked at a length scale equal to the lowest altitude which those electrons reach before reflecting (as explained in the review by Connerney et al., 2004), i.e approximately 200 km. Therefore, since both the precipitating electron flux and atmospheric density generally vary laterally on scales larger than ∼200 km (Mitchell et al., 2001; Bougher et al., 1990), provided the electron's drift distance during one bounce period is small compared to 200 km, we can be sure that the downward-traveling and upward-traveling electron populations experience approximately the same magnetic and neutral density environment and are therefore comparable for our analysis. We now calculate typical bounce times and examine the magnitude of each plasma drift separately to determine its importance.

Using a similar formalism as in Section 4, it can be shown that the round-trip time of the electron T_{bounce} is given by

$$T_{\text{bounce}} = \int_{\text{path}} \frac{\mathrm{d}s}{v(s)} = 2\int_0^{x_r} \frac{\sec\alpha(x')\,\mathrm{d}x'}{v(x')} = 2\int_0^{x_r} \frac{\mathrm{d}x'}{\sqrt{\frac{2(U_0+eEx')}{m_{\text{electron}}}}\sqrt{1-\frac{B(x')\sin^2\alpha_0}{B_0(1+\frac{eEx'}{U_0})}}}, \tag{20}$$

where v is the electron's changing velocity and E is the assumed constant electric field component parallel to the magnetic field line. The bounce time is dependent mainly on particle energy, reflection altitude and electric field, independent of absolute magnetic field strength but weakly dependent on the exponent by which the field decreases with distance from the magnetized crust. Fig. 13 shows round-trip bounce times for electrons with energies of 113, 313 eV (representing the approximate centers of the lowest and highest energy channel we consider) for an exponent of 2.2 (Brain et al., 2003) (exponents of 1.6, 2.8 resulted in <10% differences) and a range of parallel electric field values from −0.5 to 0.5 mV/m. These electric field extrema are an order of magnitude larger than typically fitted for in the data and comparable to the very largest values, seen occasionally on the boundaries of magnetic cusp regions. As can be seen, round trip bounce times can be up to 0.5 s in the case of the lowest energy channel and a very strong radially positive electric field, but are typically less than 0.3 s compared to the MGS ER pitch angle distribution integration time of 2–8 s for these energies (Mitchell et al., 2001).

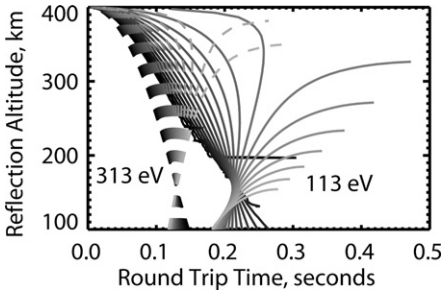

Fig. 13. Time taken for electrons' round trip from spacecraft to mirror point and back, plotted as a function of reflection altitude for electrons in the 113 eV (solid lines) and 313 eV (dashed lines) channels with parallel electric fields of −0.5 to 0.5 mV/m in increments of 0.05 mV/m with black representing −0.5 mV/m and the lightest gray representing 0.5 mV/m. As can be seen, strong enough negative (positive) electric fields can impose a lower (upper) bound on reflection altitudes.

Using equations of force and motion in SI units, it can be shown (Parks, 2004, chapter 4) that particles of charge q and mass m in a gravitational field have a constant drift velocity $\overrightarrow{W_g}$:

$$\overrightarrow{W_g} = \frac{m}{q}\frac{\vec{g}\times\vec{B}}{B^2}, \tag{21}$$

where $\vec{g}$ is the acceleration due to gravity. At spacecraft altitudes, $|\vec{g}| = 2.78\,\mathrm{m\,s^{-2}}$, typically $B > 10$ nT, so $W_g <$ 2 mm/s, giving miniscule drift distances of <1 mm, allowing this effect to be ignored.

Much like the gravitational drift but stronger, the external forced on a charge particle caused by the component of the electric field $\vec{E}$ perpendicular to the magnetic field brings about a constant drift velocity $\overrightarrow{W_E}$

$$\overrightarrow{W_E} = \frac{\vec{E}\times\vec{B}}{B^2}. \tag{22}$$

Thus, assuming a round-trip bounce time of 0.3 s and a minimum magnetic field of 10 nT, the drift distance in km, $D = 30|E|$ where E is in mV/m. Although we have no direct way to measure the component of the electric field perpendicular to the magnetic field, typical average parallel electric fields between the spacecraft at 400 km and exobase are found to be

<0.4 mV/m ∼ 98% of the time, regardless of the geometry. If perpendicular fields have comparable magnitudes, then electric field drifts should be <∼10 km under almost all conditions, and thus can safely be ignored in a statistical sense.

A similar analysis shows that the forces that arise from the component of the gradient of the magnetic field that is perpendicular to the field itself, i.e. the curvature, also causes charged particles to drift, with velocity $\overrightarrow{W_{\nabla B}}$:

$$\overrightarrow{W_{\nabla B}} = \frac{m}{2qB^4}\vec{B} \times \vec{\nabla} B^2 \left(v_{\parallel}^2 + \frac{v_{\perp}^2}{2} \right), \tag{23}$$

where $v_{\parallel}$ and $v_{\perp}$ are the components of the electron's velocity parallel and perpendicular to the magnetic field respectively. If we take the worst case where $v = v_{\parallel}$ and $\vec{B}$ is exactly perpendicular to $\vec{\nabla} B^2$, then $\overrightarrow{W_{\nabla B}} \sim U' \nabla B / B^2$ where $|\vec{\nabla} B|$ is written as ∇B and U' is the electron's energy in eV. We estimate the average value of $\nabla B / B^2$ between the spacecraft and absorption altitudes by taking typical values of ∇B and B from the lateral magnetic gradient map of Connerney et al. (2005) and the potential field model of Cain et al. (2003). In the weakest crustal field regions, $\nabla B \sim 0.005$ nT/km and $B \sim 10$ nT, so $W_{\nabla B} \sim 15$ km/s (<3 km drift) for 300 eV electrons. In the strongest field regions, $\nabla B \sim 0.5$ nT/km and $B \sim 200$ nT, so $W_{\nabla B} \sim 4$ km/s (<1 km drift). Hence the uncertainties due to magnetic curvature/gradient drift are negligible and may also be safely ignored.

7. Solving for atmospheric and magnetic profile parameters

7.1. Loss cone sensitivity to electron scattering depth

If we are to use this model along with observed loss cones to constrain properties of the magnetic field profile an electron follows or the neutral density profile it travels through, we must understand how sensitive different parts of the loss cone are to these properties. To do this we recall Eq. (13): $P_{\text{surv}} = e^{-D}$, where D is the electron's effective scattering depth.

This scattering depth D is a function of all the variables we can either assume knowledge of or would like to measure, e.g., electron–neutral impact cross-sections, densities and scale heights of each neutral species, and crustal magnetic field magnitudes at different altitudes. The accuracy to which we can determine any of these quantities is related to how well we can determine D. To investigate how measurement errors in P_{surv} affect fractional errors in D, we may differentiate P_{surv} with respect to D:

$$\frac{\partial P_{\text{surv}}}{\partial D} = -\exp[-D] = -P_{\text{surv}}.$$

Discretizing the differentials into uncertainties gives

$$\Rightarrow \quad \frac{\Delta D}{D} = \frac{\Delta P_{\text{surv}}}{P_{\text{surv}} \ln P_{\text{surv}}}. \tag{24}$$

As shown in Fig. 14, the fractional error in D, in units of ΔP_{surv} (i.e. $\Delta D/(D\Delta P_{\text{surv}})$) is nonlinearly dependent on P_{surv}, with its minimum error of e occurring at $P_{\text{surv}} = 1/e$ or $D = 1$;

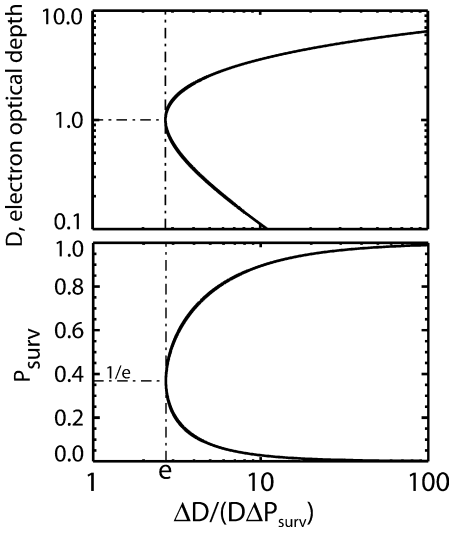

Fig. 14. Dependence of the fractional error in the electron 'scattering depth,' normalized by the error in the electron's probability, P_{surv}, of surviving the round trip to the reflection point and back (i.e. $\Delta D/(D\Delta P_{\text{surv}})$), upon P_{surv} (top) and upon the value of the scattering depth (bottom).

i.e. the minimum error in the electron scattering depth, which is found by measuring P_{surv}, occurs when the scattering depth is unity. Thus we may define a useful range of values of P_{surv} that we should accept when fitting our model to a measured loss cone. For our purposes we (somewhat arbitrarily) define our upper limit of $\Delta D/D$ to be twice its minimum value ($2e$ in units of ΔP_{surv}), thus we only use values of P_{surv} between 0.07 and 0.79 in determining D (which then must lie between 0.24 and 2.69). Values much above or below this range result in very large errors.

7.2. Loss cone sensitivity to altitude

If we wish to consider a specific variable (call it y) upon which D depends, we simply apply the chain rule to Eq. (24) to get an expression for the uncertainty in y:

$$\Delta y = \Delta P_{\text{surv}} \frac{\partial y}{\partial D} e^{D}. \tag{25}$$

For our purposes, y may be any parameter describing an aspect of the magnetic or neutral density profile. This equation is used in the two companion papers to this one (Lillis et al., 2008a, 2008b) to evaluate loss cone sensitivity to magnetic or neutral density parameters. Next we address the range of altitudes at which we can constrain these parameters.

As stated already, the objective is to fit the adiabatic loss cone model to the measured loss cones in the MAG/ER dataset to constrain the neutral densities and remote magnetic field magnitudes below the spacecraft. Clearly the field strength or density can only be probed in the range of altitudes over which the loss cone is formed, which, in the typical case shown in Fig. 8, is approximately 150–250 km altitude. However, we need to answer the following questions:

(1) Is this range true in general for all combinations of magnetic field and neutral density we are likely to see at Mars?

(2) If not, how does it vary with those factors?
(3) Within the range, where is the altitude of greatest sensitivity and how does the sensitivity worsen as we move above or below that altitude?

To answer these questions, we shall use the formalism set out in Section 5. In Fig. 15, using Eqs. (13) and (24), we examine how the altitude of greatest sensitivity (i.e. that where D for the electron's round trip is equal to unity) depends on the vertical magnetic and density profiles. We see that, as the magnetic field below the spacecraft gets stronger, the loss cone forms nearer to 0° pitch angle. The electrons forming the loss cone here start with a smaller pitch angle and hence will have traversed a smaller column depth of atmosphere upon reaching a given altitude, than will the higher-initial-pitch-angle electrons forming the loss cone produced by a shallower magnetic profile (i.e. weaker field below the spacecraft). Thus the loss cone-forming electrons in the strong field case will reach the same scattering depth at a lower altitude than those in the weak field case. We also see in Fig. 15 that, as expected, electrons reach a given fixed scattering depth at a higher altitude when the neutral density profile is higher, i.e. a thicker atmosphere absorbs electrons at a higher altitude. This altitude dependence of maximum sensitivity is an important factor in determining how to most appropriately present magnetic field or neutral density results, as shown in the two companion papers to this one (Lillis et al., 2008a, 2008b).

7.3. The coupled nature of the magnetic and neutral profiles

It must be pointed out that the vertical magnetic and neutral density profiles are non-orthogonal factors determining the shape of the adiabatic loss cone, i.e. the result of changing one can be indistinguishable from changing the other. To illustrate this, in the middle left panel of Fig. 15, the solid yellow and dashed green lines, calculated using different magnetic and neutral density profiles, are indistinguishable within the typical errors of measured loss cones. Thus, we must always assume *a priori* knowledge of one profile in order to solve for any characteristic(s) of the other. This presents a problem because of course we never have perfect knowledge of either profile. Let us now examine the effects of each profile's uncertainty in turn.

Due to the scarcity of neutral density measurements, particularly species-specific measurements, our knowledge of the neutral density profile is relatively poor below 180 km and very poor above 180 km, beyond what the MTGCM will predict. However, for a given fixed magnetic profile, the shift in loss cone position between the minimum and maximum MTGCM atmospheres is quite small compared to the shift between steep and shallow magnetic profiles, as shown in Fig. 15. In other words, the neutral density profile responsible for electron absorption in a given loss cone is highly uncertain (probably a factor of several above 200 km), but we know that even these large uncertainties will not result in large shifts in the loss cone position.

Our knowledge of the magnetic profile on the martian night side is highly dependent on geographic location. In regions where the permanent crustal field is much stronger than the temporally variable induced magnetotail field, the magnetic profile from 100 to 400 km can be well represented by equivalent source and spherical harmonic models of the vector magnetic field (e.g., Purucker et al., 2000; Langlais et al., 2004; Arkani-Hamed, 2001, 2002, 2004; Cain et al., 2003; Whaler and Purucker, 2005). But in regions where the magnetotail field is comparable to or stronger than the crustal field at or below 250 km, the fixed spherical harmonic models are unreliable in the altitude range of electron absorption. Thus, in these regions, even though the magnetometer can measure the instantaneous direction and magnitude of the magnetic field at ~400 km, the fractional uncertainty in the magnetic profile is large in the altitude range where the profile is most important.

This dependence of the uncertainty in magnetic profile on crustal field strength has consequences for the accurate prediction of loss cone shapes, as clearly demonstrated in Fig. 16. In the strong field case, the uncertainty in the magnetic profile caused by the varying magnetotail field makes little difference to the predicted loss cone shape, whereas in the weak field case, the same uncertainties can make a large difference.

It is clear from the above discussion that it would be unwise to initially attempt to solve for characteristics of the density profile in any but the strongest crustal field regions. It is similarly clear that, by initially assuming some median MTGCM atmosphere and solving for characteristics of the magnetic profile, our results would be biased by a probably small but ultimately indeterminate amount, since we would have no idea how far our assumption was from the true mean neutral density profile, given the large uncertainties in the MTGCM. Since the effect of parallel electric fields are distinct from those of the neutral atmosphere or magnetic field, we should be able to solve separately for their effects whether we assume prior knowledge of the neutral density or magnetic field profiles.

8. Method of solving for magnetic, electric and neutral density properties of the near-Mars environment

We have outlined a theoretical description of the dependence of loss cone shape on the neutral atmosphere, the magnetic field magnitude, and the average parallel electric field between 400 and approx 200 km. Within the uncertainties in the loss cone shape, the neutral atmosphere can be adequately parameterized by a multiplicative factor by which to scale the MTGCM (Lillis et al., 2008a). The magnetic field magnitude profile can be adequately parameterized by its known value at the spacecraft orbital altitude (370–430 km) and its value near 180 km, as shown in Lillis et al. (2008b). The parallel electric field can be parameterized by a single average value, as discussed in Section 5.2.

Thus we have three unknowns (essentially mass density and magnetic field magnitude near 180 km, plus average electric field) and loss cone shape data from three adjacent energy channels (90–145, 145–248, 248–400 eV) with which to solve for them. However, as discussed in earlier sections, the effects of the magnetic and neutral density profiles on these shapes are often indistinguishable from each other and always independent

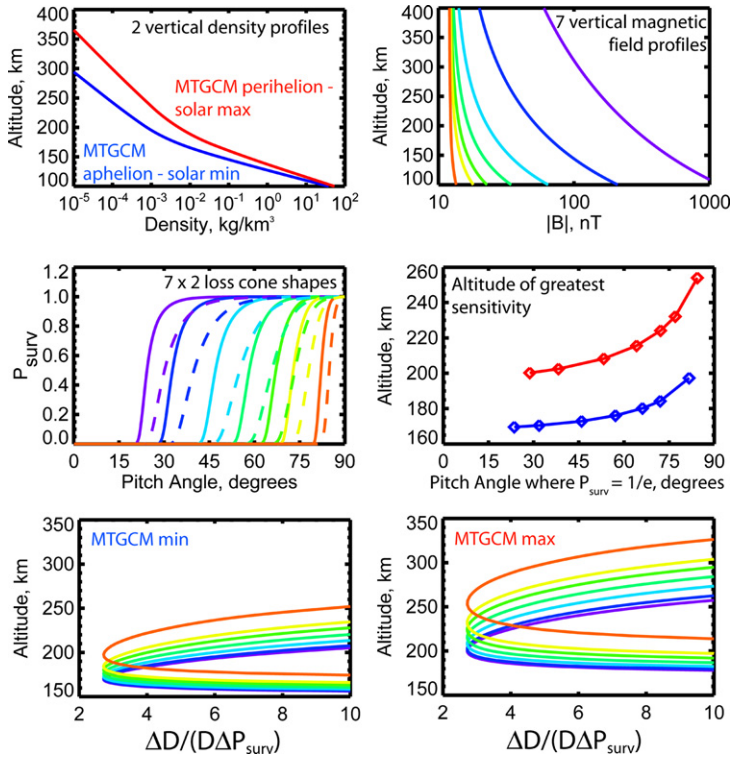

Fig. 15. Altitude sensitivity of loss cones as a function of magnetic field and neutral density profiles. Upper left panel plots 2 possible extrema MTGCM atmospheric mass density profiles: solar minimum-aphelion versus solar maximum-perihelion conditions. Upper right panel plots 7 possible magnetic field profiles. The 14 resulting loss cones are shown in the middle left panel, with solid and dashed lines representing the min and max atmosphere cases respectively. The 2 lower panels plot $\Delta D/D$ versus altitude for the 2 atmosphere cases. Finally the middle right panel plots the altitude of greatest sensitivity versus loss cone angle (i.e. the altitude and initial pitch angle where $P_{\mathrm{surv}} = 1/e$ and $D = 1$) for the 2 atmosphere cases.

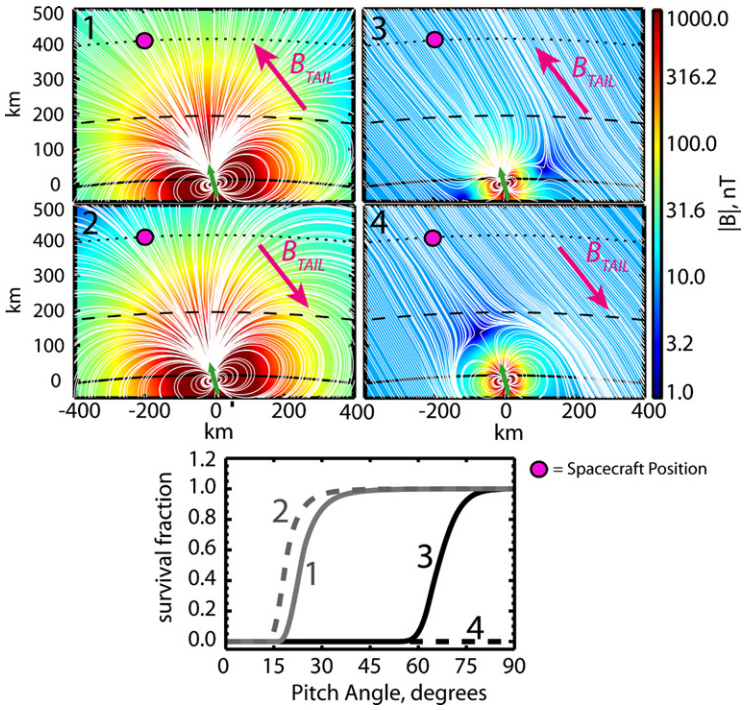

Fig. 16. Relative importance of a variable magnetotail field in determining loss cone shapes. The top and middle left panels show the magnetic field geometry/topology resulting from the superposition of a 1.5×10^{16} A/m^2 dipole field and an 8 nT magnetotail field, oriented in two opposite directions. The top and middle right panels show an identical situation except the dipole is 100 times weaker. The pink dot is the position of the spacecraft and the pink arrow is the direction of the magnetotail field. The solid black line, dashed black line and dotted black line represent the surface, the exobase at 180 km and the spacecraft orbit at 400 km, respectively. The small green arrow represents the direction of the magnetic dipole. The bottom panel shows the resulting adiabatic loss cones resulting from precipitating electrons in the 4 field geometries shown.

of energy, so we must make assumptions a priori to solve for mass densities or magnetic field magnitudes. Thus we choose to proceed from the position of greatest knowledge and continue in an iterative manner.

In Lillis et al. (2008a), we consider the small fraction of regions (approximately 2% of the planet, entirely in the Southern Hemisphere) where the magnetic field lines are open to the solar wind and the radial component of the crustal field is more than 50 nT. We consider only the times when spacecraft magnetometer measurements agree with the spherical harmonic crustal magnetic field model of Cain et al. (2003). We assume knowledge of the magnetic profile and solve for the neutral density profile independent of the MTGCM using a 3-parameter, 2-species (O, CO_2) isothermal atmospheric model, while correcting for the mean effect of parallel electric fields in each geographic region. This gives us an estimate of the neutral mass density in the absorption region, though it provides no meaningful information about temperature or densities of individual species, implying that, for this technique and data set, the atmosphere may be adequately parameterized by a single multiplicative factor by which to scale the MTGCM profiles.

In Lillis et al. (2008b), we use the mean value of this multiplicative factor and multiply it by a solar moderate, equinox MTGCM atmosphere to give us a reliable mean density profile to use to simultaneously solve for the crustal magnetic field magnitude and average electric field in the absorption region all over the planet. With >2 million measurements over 4 martian years, all variation due to changes in the atmospheric density profile averages out close to zero and we are left with a mean value for the crustal magnetic field in all geographic regions where loss cones form, at 185 km above the planet's surface. These are combined into a highly sensitive global map of crustal magnetic field. We find that parallel electric fields are typically very small (<0.1 mV/m) but can be substantially higher at the edges of magnetic cusps in strong crustal field regions.

With knowledge of the average crustal magnetic field in the absorption region and magnetometer measurements at ~400 km, we may reconstruct the likely magnetic profile to solve for a calibrated neutral density in the absorption region for all the observed loss cones. This work greatly expands geographically the areas of Mars for which neutral densities can be estimated and should result shortly in manuscript submission.

9. Concluding remarks

In this paper we have presented a theoretical framework for understanding the formation of electron loss cones in the near space environment of a planet with a significant atmosphere, taking account of the important physical considerations. Our analysis of the sensitivity of the technique is specific to Mars but the underlying approach is generalizable to any planetary body with an atmosphere and planetary magnetic fields which connect with the interplanetary magnetic field. The overall goal of this project is to use the above framework and strategy to arrive at three sets of results:

(1) The best possible global map of crustal magnetic field magnitude at the altitudes of greatest electron absorption (~185 km), which we shall interpret with the aid of published geological, topographical, crustal thickness and gravity studies of Mars in an attempt to constrain important parameters of Mars' thermal and magnetic history. This map is presented in Lillis et al. (2008b), along with two case studies, the first comparing the magmatic and magnetic histories of the Highland volcanoes Syrtis Major and Tyrrhena Patera and the second using the magnetic signatures and crater retention ages of the Ladon and Hellas impact basins to bracket the time at which the martian dynamo ceased permanently.

(2) A database of neutral mass densities at 180 km at 2:00 a.m. over 7 Earth years, which we shall interpret with the aid of the MTGCM. This will help us to understand the effects of seasonal and latitudinal insolation variations, the solar cycle and dust storms on the martian upper thermosphere. First results are given in Lillis et al. (2008a).

(3) A database of estimates of the average parallel electric field between ~200 km to 400 km on open magnetic field lines on the martian night side at 2 a.m. local time, over 7 Earth years, with which we can map the electric field environment of Mars geographically in this altitude range at 2 a.m. local time and determine how that environment changes with the direction of the interplanetary magnetic field (IMF) and with the seasons as Mars's axial tilt alters the relative orientation of the crustal magnetic fields with respect to the martian magnetotail.

Acknowledgments

Many thanks to Paul Withers for an extraordinarily quick, thorough and helpful review. This work was supported by NASA grants JPL 1271721-05/06 and JPL 08668-01/07.

References

Acuña, M.H., and 16 colleagues, 1992. The Mars Observer magnetic fields investigation. J. Geophys. Res. Planets 97, 7799–7914.

Acuña, M.H., and 13 colleagues, 2001. Magnetic field of Mars: Summary of results from the aerobraking and mapping orbits. J. Geophys. Res. 106, 23403–23417.

Ajello, J.M., James, G.K., Franklin, B., Howell, S., 1990. Study of electron impact excitation of argon in the extreme ultraviolet: Emission cross section of resonance lines of Ar I, Ar II. J. Phys. B At. Mol. Opt. Phys. 23, 4355–4376.

Albee, A.L., Arvidson, R.E., Palluconi, F., Thorpe, T., 2001. Overview of the Mars Global Surveyor mission. J. Geophys. Res. 106, 23291–23316.

Anderson, K.A., Lin, R.P., McCoy, J.E., McGuire, R.E., 1976. Measurements of lunar and planetary magnetic fields by reflection of low energy electrons. Space Sci. Instrum. 1, 439–470.

Arkani-Hamed, J., 2001. A 50-degree spherical harmonic model of the magnetic field of Mars. J. Geophys. Res. 106, 23197–23208.

Arkani-Hamed, J., 2002. An improved 50-degree spherical harmonic model of the magnetic field of Mars derived from both high-altitude and low-altitude datasets. J. Geophys. Res. 107 (E10), doi:10.1029/2001JE001835. 5083.

Arkani-Hamed, J., 2004. A coherent model of the crustal field of Mars. J. Geophys. Res. 109, doi:10.1029/2003JE002265. E09005.

Binder, A.P., 1998. Lunar Prospector: Overview. Science 281 (5382), 1475–1476.

Bougher, S.W., Roble, R.G., Ridley, E.C., Dickinson, R.E., 1990. The Mars thermosphere. II. General circulation with coupled dynamics and composition. J. Geophys. Res. 95, 14811–14827.

Bougher, S.W., Engle, S., Roble, R.G., Foster, B., 1999. Comparative terrestrial planet thermospheres. 2. Solar cycle variation of global structure and winds at equinox. J. Geophys. Res. 104, 16591–16611.

Bougher, S.W., Engle, S., Roble, R.G., Foster, B., 2000. Comparative terrestrial planet thermospheres. 3. Solar cycle variation of global structure and winds solstices. J. Geophys. Res. 105, 17669–17692.

Bougher, S.W., Roble, R.G., Fuller-Rowell, T.J., 2002. Simulations of the upper atmospheres of the terrestrial planets. In: Mendillo, M., Nagy, A., Waite, J.H. (Eds.), Atmospheres in the Solar System: Comparative Aeronomy. In: AGU Monographs, vol. 130. American Geophysical Union, Washington, DC, pp. 261–288.

Bougher, S.W., Bell, J.M., Murphy, J.R., Lopez-Valverde, M.A., Withers, P.G., 2006. Polar warming in the Mars thermosphere: Seasonal variations owing to changing insolation and dust distributions. Geophys. Res. Lett. 32, doi:10.1029/2005GL024059. L02203.

Bougher, S.W., Bell, J.M., Steers, B., Murphy, J.R., Keating, G.M., 2007. Winter polar warming in the Mars thermosphere. LPI Contributions 1353, 3027.

Brain, D.A., Bagenal, F., Acuna, M.H., Connerney, J.E.P., 2003. Martian magnetic morphology: Contributions from the solar wind and crust. J. Geophys. Res. 108 (A12), doi:10.1029/2002JA009482. 1424.

Brain, D.A., Halekas, J.S., Peticolas, L.M., Lin, R.P., Luhmann, J.G., Mitchell, D.L., Delory, G.T., Bougher, S.W., Acuna, M.H., Réme, H., 2006. On the origin of aurorae on Mars. Geophys. Res. Lett. 33, 1201.

Brain, D.A., Lillis, R.J., Mitchell, D.L., Halekas, J.S., Lin, R.P., 2007. Electron pitch angle distributions as indicators of magnetic field topology near Mars. J. Geophys. Res. 112, doi:10.1029/2007JA012435. A09201.

Burnett, T., Rountree, S.P., 1979. Differential and total cross sections for electron-impact ionization of atomic oxygen. Phys. Rev. A 20, 1468–1473.

Butler, S.T., Buckingham, M.J., 1962. Energy loss of a fast ion in plasma. Phys. Rev. 1261, 1–4.

Cain, J.C., Ferguson, B.B., Mazoni, D., 2003. An $n = 90$ internal potential function of the martian crustal magnetic field. J. Geophys. Res. 107 (E2), doi:10.1029/2000JE001487. 5008.

Chilton, J.E., Lin, C.C., 1999. Measurement of electron-impact excitation into the $3p^5 3d$ and $3p^5 5s$ levels of argon using Fourier-transform spectroscopy. Phys. Rev. A 605, 3712–3721.

Connerney, J.E.P., Acuna, M.H., Ness, N.F., Spohn, T., Schubert, G., 2004. Mars crustal magnetism. Space Sci. Rev. 1, 1–33.

Connerney, J.E.P., Acuña, M.H., Ness, N.F., Kletetschka, G., Mitchell, D.L., Lin, R.P., Reme, H., 2005. Tectonic implications of Mars crustal magnetism. Proc. Natl. Acad. Sci. USA 102, 14970–14975.

Cvejanovic, D., Crowe, A., 1997. Differential cross sections for elastic scattering of electrons from argon and krypton as a continuous function of energy. J. Phys. B At. Mol. Opt. Phys. 30, 2873–2887.

Dalgarno, A., McElroy, M.B., Moffett, R.J., 1963. Electron temperatures in the ionosphere. Planet. Space Sci. 11, 463–484.

Espley, J.R., Delory, G.T., Cloutier, P.A., 2006. Initial observations of low-frequency magnetic fluctuations in the martian ionosphere. J. Geophys. Res. 111, doi:10.1029/2005JE002587. E06S22.

Ferguson, B.B., Cain, J.C., Crider, D.H., Brain, D.A., Harnett, E.M., 2005. External fields on the nightside of Mars at Mars Global Surveyor mapping altitudes. Geophys. Res. Lett. 32, 16, doi:10.1029/2004GL021964.

Halekas, J.S., 2003. The origins of lunar crustal magnetic fields. Ph.D. thesis, UC Berkeley.

Halekas, J.S., Mitchell, D.L., Lin, R.P., Frey, S., Hood, L.L., Acuña, M.H., Binder, A.B., 2001. Mapping of crustal magnetic anomalies on the lunar near side by the Lunar Prospector electron reflectometer. J. Geophys. Res. 106, 27841–27852.

Halekas, J.S., Mitchell, D.L., Lin, R.P., Hood, L.L., Acuña, M.H., Binder, A.B., 2002. Demagnetization signatures of lunar impact craters. Geophys. Res. Lett. 29 (13), doi:10.1029/2001GL013924. 1645.

Halekas, J.S., Lin, R.P., Mitchell, D.L., 2003. Magnetic fields of lunar multiring impact basins. Meteorit. Planet. Sci. 38, 565–578.

Halekas, J.S., Brain, D.A., Lillis, R.J., Fillingim, M.O., Mitchell, D.L., Lin, R.P., 2006. Current sheets at low altitudes in the martian magnetotail. Geophys. Res. Lett. 33, 13, doi:10.1029/2006GL026229.

Itikawa, Y., 2002. Cross sections for electron collisions with carbon dioxide. J. Phys. Chem. Ref. Data 31 (3), doi:10.1063/1.1481879#.

Langlais, B., Purucker, M.E., Mandea, M., 2004. Crustal magnetic field of Mars. J. Geophys. Res. 109, doi:10.1029/2003JE002048. E02008.

Lillis, R.J., Mitchell, D.L., Lin, R.P., Connerney, J.E.P., Acuña, M.H., 2004. Mapping crustal magnetic fields at Mars using electron reflectometry. Geophys. Res. Lett. 31, doi:10.1029/2004GL020189. L15702.

Lillis, R.J., Engel, J.H., Mitchell, D.L., Brain, D.A., Lin, R.P., Bougher, S.W., Acuna, M.H., 2005. Probing upper thermospheric neutral densities at Mars using electron reflectometry. Geophys. Res. Lett. 32, doi:10.1029/2005GL024337. L23204.

Lillis, R.J., Manga, M., Mitchell, D.L., Lin, R.P., Acuña, M.H., 2006. Unusual magnetic signature of the Hadriaca Patera Volcano: Implications for early Mars. Geophys. Res. Lett. 33, doi:10.1029/2005GL024905. L03202.

Lillis, R.J., Bougher, S.W., Mitchell, D.L., Brain, D.A., Lin, R.P., Acuña, M.H., 2008a. Continuous monitoring of nightside upper thermospheric mass densities in the martian southern hemisphere over 4 martian years using electron reflectometry. Icarus 194, 562–574.

Lillis, R.J., Frey, H.V., Manga, M., Mitchell, D.L., Lin, R.P., Acuña, M.H., Bougher, S.W., 2008b. Improved crustal magnetic field map of Mars from electron reflectometry: Highland volcano magmatic history and the end of the martian dynamo. Icarus 194, 575–596.

Lin, R.P., 1979. High spatial resolution measurements of surface magnetic fields of the lunar frontside. Proc. Lunar Sci. Conf. 10, 2259–2264.

Lundin, R., and 22 colleagues, 2006. Plasma acceleration above martian magnetic anomalies. Science 311, 980–983.

Ma, Y., Nagy, A., Hansen, K., DeZeeuw, D., Gombosi, T., 2002. Three-dimensional multispecies MHD studies of the solar wind interaction with Mars in the presence of crustal fields. J. Geophys. Res. 107, doi:10.1029/2002JA009293.

Mitchell, D.L., Lin, R.P., Mazelle, C., Rème, H., Cloutier, P.A., Connerney, J.E.P., Acuña, M.H., Ness, N.F., 2001. Probing Mars' crustal magnetic field and ionosphere with the MGS Electron Reflectometer. J. Geophys. Res. 106, 23419–23427.

Mitchell, D.L., Lillis, R.J., Lin, R.P., Connerney, J.E.P., Acuña, M.H., 2007. A global map of Mars' crustal magnetic field based on electron reflectometer. J. Geophys. Res. 112 (E1), doi:10.1029/2005JE002564. E0100.

Nagy, A.F., and 15 colleagues, 2004. The plasma environment of Mars. Space Sci. Rev., 1–82.

Nier, A.O., McElroy, M.B., 1977. Composition and structure of Mars' upper atmosphere—Results from the neutral mass spectrometers on Viking 1 and 2. J. Geophys. Res. 82, 4341–4349.

Opal, C.B., Peterson, W.K., Beaty, E.C., 1971. Measurements of secondary-electron spectra produced by electron impact ionization on a number of simple gases. J. Chem. Phys. 33, 4100–4106.

Parks, G., 2004. Physics of Space Plasmas. Westview, Cambridge, MA.

Porter, H.S., Jump, F.W., 1978. Analytic total angular elastic electron impact cross sections for planetary atmospheres, NASA Publication CSC/TM-78/6017.

Porter, H.S., Varosi, F., Mayr, H.G., 1987. Iterative solution of the multistream electron transport equation. 1. Comparison with laboratory beam injection experiments. J. Geophys. Res. 92, 5933–5959.

Purucker, M.E., Ravat, D., Frey, H., Voorhies, C., Sabaka, T., Acuña, M.H., 2000. An altitude-normalized magnetic map of Mars and its interpretation. Geophys. Res. Lett. 27, 2449–2452.

Shyn, T.W., Sharp, W.E., 1979. Doubly differential cross section of secondary electrons ejected from gases by electron impact: 50–400 eV on CO_2. Phys. Rev. A 20, 2332–2339.

Sung, K., Fox, J.L., 2000. Electron impact cross sections for use in modeling the ionospheres/thermospheres of the Earth and planets. Eos (Fall Suppl.) 81 (48). SA52A-11.

Tyler, G.L., Balmino, G., Hinson, D.P., Sjogren, W.L., Smith, D.E., Simpson, R.A., Asmar, S.W., Priest, P., Twicken, J.D., 2001. Radio science observations with Mars Global Surveyor: Orbit insertion through one Mars year in mapping orbit, 2001. J. Geophys. Res. 106 (E10), 23327–23348.

Withers, P., 2006. Mars Global Surveyor and Mars Odyssey Accelerometer observations of the martian upper atmosphere during aerobraking. Geophys. Res. Lett. 33, doi:10.1029/2005GL024447. L02201.

Whaler, K.A., Purucker, M.E., 2005. A spatially continuous magnetization model for Mars. J. Geophys. Res. 110 (E9), doi:10.1029/2004JE002393. E09001.